Wideband Polarization Conversion with the Synergy of Waveguide and Spoof Surface Plasmon Polariton Modes

Yongfeng Li,[1,*] Yongqiang Pang,[1,2] Jiafu Wang,[1] Qiqi Zheng,[1] Maochang Feng,[1] Hua Ma,[1] Jieqiu Zhang,[1] Zhuo Xu,[2] and Shaobo Qu[1,†]

[1]*College of Science, Air Force Engineering University, Xi'an 710051, People's Republic of China*
[2]*Electronic Materials Research Laboratory, Key Laboratory of Ministry of Education, Xi'an Jiao-tong University, Xi'an 710049, People's Republic of China*

(Received 5 May 2017; published 3 December 2018)

We propose to achieve wideband, high-efficiency polarization conversions of transmission waves with the synergy of the waveguide and spoof surface plasmon polariton (SSPP) modes. High-efficiency transmissions based on SSPP mode coupling and waveguide mode coupling are designed in two orthogonal directions, respectively. By designing the nonlinear dispersions of the SSPP and waveguide modes, the required phase differences for polarization conversion can be obtained in a wide frequency range. To verify this principle, two different polarization conversion metamaterials (PCMs) are designed and fabricated for linear-to-circular (LTC) and circular-to-circular (CTC) polarization conversions, respectively. It is found that the LTC polarization conversion transmittivity of the LTC PCM is greater than −0.5 dB from 7 to 12.6 GHz, and the cross-polarization transmittivity of the CTC PCM for a circularly polarized incidence wave is greater than −0.5 dB in the frequency range of 7–11 GHz, showing a wide band feature.

DOI: 10.1103/PhysRevApplied.10.064002

I. INTRODUCTION

Polarization is one of the fundamental properties of electromagnetic (EM) waves [1,2]. It is of great significance to have the capability of freely controlling polarization of EM waves and researchers have devoted much time to the realization of polarization manipulation. Polarization conversion is the first step, including polarization rotation, linear-to-circular, and circular-to-linear polarization conversions. In the visible spectrum, polarization conversion has always been realized using waveplates made of birefringent materials such as crystalline solids and liquid crystals [3,4]. Bulky configuration and narrow working bandwidths prevent such waveplates from being integrated into micro-optical systems. In the microwave regime, polarization conversions usually resort to ferrite phase shifter and multilayered gating polarizers. With the rapid development of EM metamaterials, polarization manipulations can be also achieved using anisotropic or chiral metamaterials [5,6], yet still with thickness limitations for the wideband purposes. In recent years, metasurfaces, the two-dimensional (2D) version of metamaterials, have provided another way of polarization manipulation. With the concept of phase "discontinuities" in the metasurfaces, the phase shift desired for polarization conversion can be easily achieved. The ultra-thin and low-loss metasurface-based polarization converters [7–24] have attracted great interest from researchers. L. Zhou *et al.* proposed an anisotropic ultrathin transparent metasurface for polarization conversion and rotation within different transmission mechanisms for the two incident polarizations [20]. In 2017, they demonstrated a microwave transmissive Pancharatnam-Berry (PB) metasurface with a thickness of approximately λ/8 exhibiting a maximum photonic spin Hall effect efficiency of approximately 91% [21]. Pfeiffer and Grbic proposed and demonstrated Huygens' metasurfaces composed of 2D arrays of polarizable particles that provide both electric and magnetic polarization currents to generate prescribed wave fronts, which can realize high-efficiency polarization manipulations of the transmitted waves [22,23]. Bai *et al*. achieved high-efficiency cross-polarization transmissions under circularly polarized (CP) wave incidence based on Fabry-Perot resonance using a multilayered metasurface [24]. However, the wideband polarization conversion efficiency is not so satisfactory, especially for the transmitted waves. In our previous works, high-efficiency polarization conversion transmissions were achieved based on spoof surface plasmon polariton (SSPP) modes [25–29] in which the desired phase difference was produced between the SSPP mode and the free-space wave [30,31]. Therefore, the thickness of the polarization conversion metamaterial depends entirely on the spatial dispersion modulation of the SSPP.

We propose to achieve wideband and high-efficiency polarization conversion transmission with the synergy of

*lyf130217@163.com
†qushaobo@126.com

a slow wave and a fast wave. In detail, high-efficiency transmission based on SSPP mode coupling is designed for one linear polarization component, which is a slow wave mode transmission. For the orthogonal polarization component, high-efficiency transmission as a fast wave mode is achieved based on waveguide mode coupling. Compared with other schemes of polarization conversion, our scheme can be potentially thin because of the strong dispersion of the SSPP and waveguide modes. Furthermore, wideband and high-efficiency polarization conversion based on the proposed device in transmission geometry can be achieved due to the engineered dispersion cancellation of the two nonlinearly dispersive modes.

II. THEORY

The working principle diagram of the proposed polarization conversion metamaterials (PCMs) is illustrated in Fig. 1. It is composed of the metallic plate array (MPA) along the y direction and a metallic fishbone array (MFA) along the x direction. The incidence x polarized wave propagates in the MPA as the waveguide mode with a smaller k as shown in Fig. 1(a). The propagation constant of the waveguide mode along the z direction k_z can be expressed as

$$k_z^2 = k_0^2 - \left(\frac{n\pi}{p_y}\right)^2, \quad n = 1, 2, \tag{1}$$

where k_0 is the propagation constant of the free-space wave, the inner height of the planar waveguide is p_y, and n is the positive integer. Accordingly, the resulted phase accumulation is $\Delta\varphi_{xx} = k_z t$. The dispersion diagrams of the x polarized wave in the MPA with different repetition periods, $p_y = 22$, 27, and 32 mm, are given in Fig. 2(a), in which the red solid line is for the free-space wave. It is found that the wave-vector component k_z in the MPA for the x polarized incidence wave is less than the wave-vector of the free-space wave k_0. They are fundamental modes of the waveguide corresponding to the mode number $n = 1$. The wave-vector component k_z of the waveguide mode increases with increasing repetition period p_y. The simulated transmissions of the MPA under the x polarized wave's normal incidence are given in Fig. 2(c). It is observed that the x polarized wave is highly transmitted above the frequencies $f = 4.7$, 5.6, and 6.9 GHz, which exactly correspond to the cut-off frequencies of the waveguide's fundamental mode. In addition, the transmissions are suppressed above the frequencies of 13.4, 13.7, and 14.2 GHz. This is because at these frequencies, the phase accumulations of the waveguide mode in the MPA $k_z t$ are exactly equal to π. Thus, reflection enhancement results.

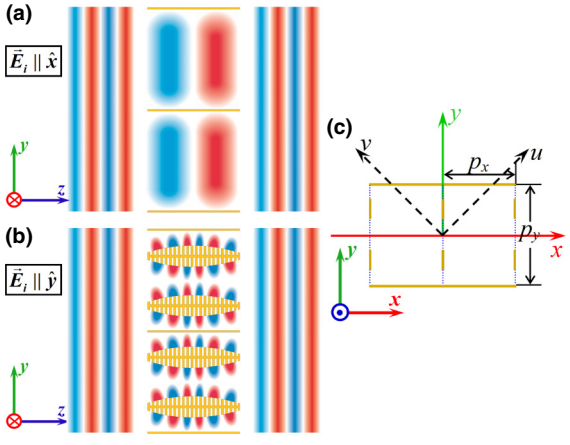

FIG. 1. Working principle diagram of the proposed PCMs. (a) x polarized wave's incidence. (b) y polarized wave's incidence. (c) Front view of the proposed PCM.

The MFA along the x direction can efficiently couple the y polarized incidence wave into SSPP on the metallic blade structure with a larger k in the PCMs as shown in Fig. 1(b). Thus, the resulting phase accumulation is $\Delta\varphi_{yy} = \int k_{\mathrm{SSPP}}(z)dz$, where $k_{\mathrm{SSPP}}(z)$ is the propagation constant of the SSPP mode. Figure 2(b) gives the dispersion diagrams of the metallic blade structure with different blade lengths, $h = 2.2$, 2.7, and 3.2 mm, for the y polarized incidence wave, in which the red solid line represents the free-space wave. The inset illustrates the proposed metallic blade structure, which is sandwiched between two 0.6-mm-thick F4B ($\epsilon_r = 2.65$, $\tan\delta = 0.001$) dielectric substrates. The metallic blade length is h, the blade width is w, the blade repetition period is p, and the width of the metallic ridge stripe along the z direction is w_s. From the f-k relations, the dispersion curves of the waves in the metallic blade structure arrays are below the light line. The k is larger than that for the waves in free space at a fixed frequency. This indicates that the metallic blade structure is capable of confining electromagnetic waves on the surface. Thus, the y polarized wave propagating in the metallic blade structure array can be considered as the SSPP in GHz frequencies. The dispersion curves include two branches corresponding to the even and odd modes, respectively, and the asymptotic frequencies of the two modes are quite close to each other. Additionally, the SSPP modes will be cut off as the frequency is greater than the asymptotic frequency. The asymptotic frequency together with the propagation constant at a fixed frequency can all be easily tailored by changing the metallic blade length h. In detail, the propagation constant of the SSPP increases with increasing blade length h, and the asymptotic frequency moves toward the lower frequency as the blade length h is increased. The simulated transmissions of the metallic blade structure array with different blade lengths, $h = 2.2$, 2.7, and 3.2 mm, under the y polarized wave's normal incidence are given in Fig. 2(d). The metallic blade structure consists of 44 metallic blades. It is observed that the y polarized incidence wave can be transmitted below the frequencies $f = 14.5$, 17.2, and 21.2 GHz, which exactly

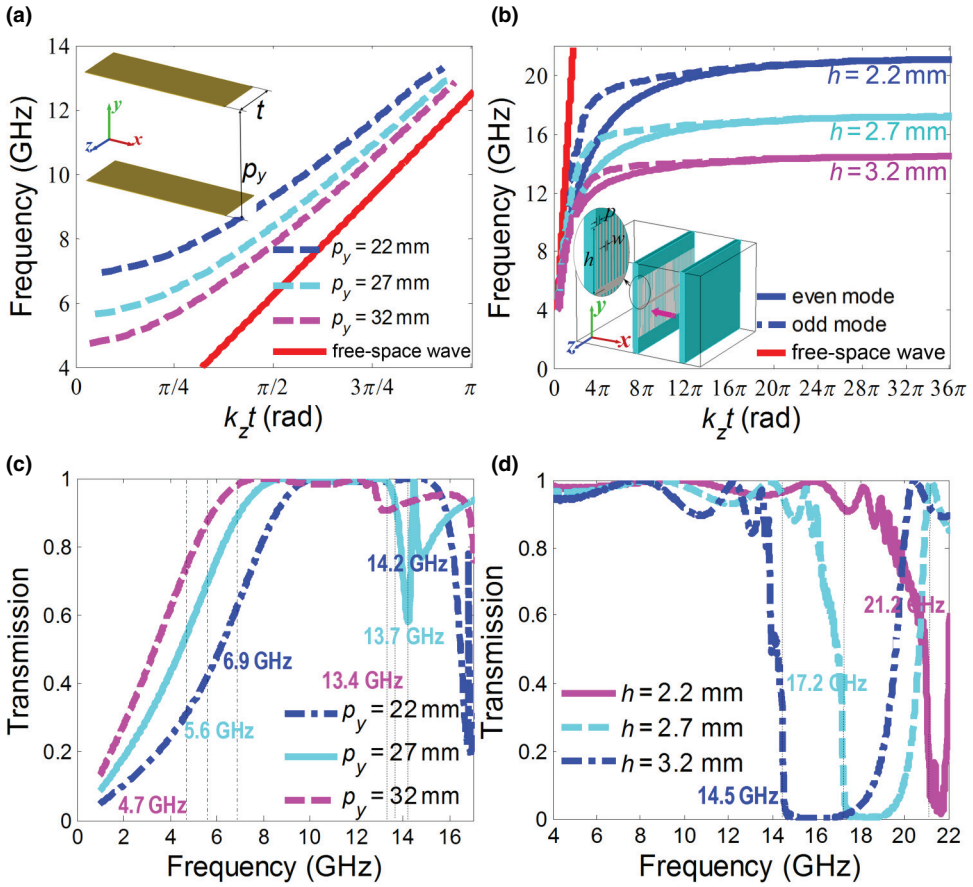

FIG. 2. (a) Dispersion diagrams of the x polarized wave in the nearly-zero-thick MPA with different repetition periods of $p_y = 22$, 27, and 32 mm. (b) Dispersion diagrams of the y polarized wave in the metallic fishbone structure array with different blade lengths of $h = 2.2$, 2.7, and 3.2 mm. (c) Simulated transmissions of the MPA with different repetition periods of $p_y = 22$, 27, and 32 mm under the x polarized wave's normal incidence. (d) Simulated transmissions of the metallic blade array with different blade lengths of $h = 2.2$, 2.7, and 3.2 mm under the y polarized wave's normal incidence.

correspond to the asymptotic frequencies of the mediated SSPPs. This indicates that the transmissions are achieved based on SSPP mode coupling on the metallic blade structure. However, the achieved transmissions are not high, especially close to the asymptotic frequencies. This is mainly attributed to the mismatch of the wave-vectors between the incidence wave and the coupled SSPP. Thus, a tapered metallic blade structure with a spatially modulated blade length called the metallic fishbone structure is designed to achieve high-efficiency transmission.

As for the proposed PCMs illustrated in Fig. 1, the phase difference between the copolarization transmissions under y and x polarized waves' normal incidence is $\Delta\varphi = \int k_{\mathrm{SPP}}(z)dz - k_z t$. Since the dispersion relationships are all nonlinearly dispersive, a fixed phase difference $\Delta\varphi$ and thus the polarization converse may be realized in a wide frequency band by designing their dispersions.

We assume that the electric field of the incidence wave is

$$\boldsymbol{E}_i = \frac{\sqrt{2}}{2} E_0 (\hat{x} + e^{i\delta}\hat{y}) e^{i\boldsymbol{k}_0 \boldsymbol{r}}, \tag{2}$$

where δ is the phase difference between the x and y components of the incidence electric field. Thus, the incidence wave is CP if the phase difference is $\delta = \pm\pi/2$, and linearly polarized (LP) as the phase difference is $\delta = \pm\pi$ or 0. In detail, the incidence wave is left-handed circularly polarized (LCP) as $\delta = \pi/2$, right-handed circularly polarized (RCP) as $\delta = -\pi/2$, u polarized as $\delta = 0$, and v polarized as $\delta = \pm\pi$. According to the Jones matrix, as the cross-polarization transmissions (t_{xy}, t_{yx}) are ignored, the electric field of the transmitted wave can be expressed as

$$\boldsymbol{E}_t = \frac{\sqrt{2}}{2} E_0 (t_{xx}\hat{x} + t_{yy} e^{i(\delta+\Delta\varphi)}\hat{y}) e^{i\boldsymbol{k}_0 \boldsymbol{r}}, \tag{3}$$

where $\Delta\varphi = \varphi_{yy} - \varphi_{xx}$ is the phase difference between the copolarization transmission coefficients under the y and x polarized waves' incidence. The amplitude and phase of the copolarization transmission coefficient under y (x) polarized wave incidence are $t_{yy\,(xx)}$ and $\varphi_{yy\,(xx)}$, respectively. If $t_{yy} \approx t_{xx} \approx 1$, we can conclude that under CP waves' incidence, the transmitted waves will be

cross-polarized as the phase difference is $\Delta\varphi = \pm\pi$, and under LP (CP) waves' incidence, the transmitted waves will be CP (LP) as the phase difference is $\Delta\varphi = \pm\pi/2$. According to this principle, we design two PCMs, respectively, for circular-to-circular (CTC) and linear-to-circular (LTC) polarization conversions in the following sections.

III. LINEAR-TO-CIRCULAR PCM

The designed LTC PCM is illustrated in Fig. 3(a). The MPA consisting of nearly-zero-thick metallic plates periodically placed along the y direction is employed to work as the planar waveguide array. The thickness of the metallic waveguide wall is d. The height between adjacent inner walls of the planar waveguide is p_y. The metallic fishbone structures placed in the y-z plane are used to couple

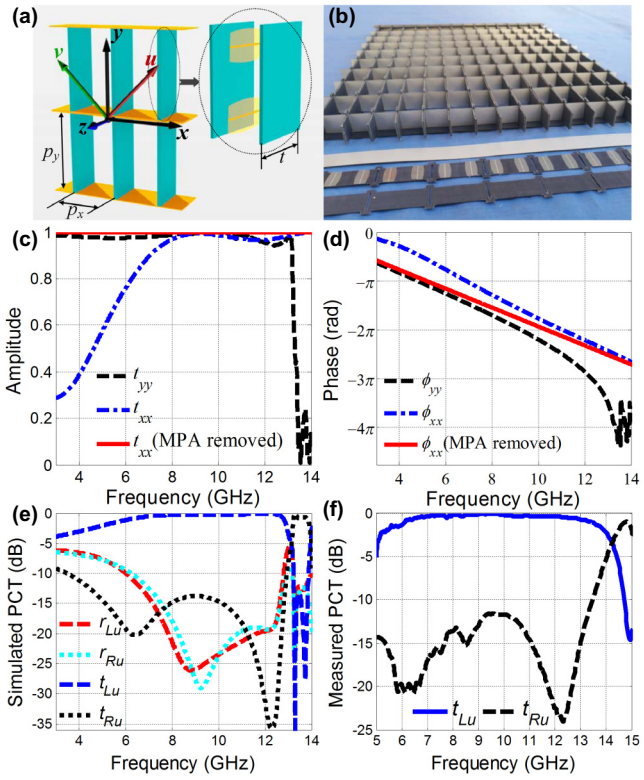

FIG. 3. (a),(b) Structural views of the LTC PCM: (a) perspective view of the designed LTC PCM ($t = 12$ mm, $p_y = 26.7$ mm, $p_x = 15$ mm, $a = 13.5$ mm, $d = 0.3$ mm, and $h = 0.6$ mm). (b) Photograph of the fabricated LTC PCM sample. (c),(d) Simulated copolarization transmission coefficients for the y and x polarized waves' normal incidence onto the designed LTC PCM together with the copolarization transmission coefficients for the x polarized wave's normal incidence onto the LTC PCM with the MPA being removed. (c) Amplitude of the simulated copolarization transmission coefficients. (d) Phase of the simulated copolarization transmission coefficients. (e) Simulated PCTs for the u polarized wave's normal incidence onto the designed LTC PCM. (f) Measured LTC PCTs for the u polarized wave's normal incidence.

and guide SSPPs, which are sandwiched between two 0.6-mm-thick F4B ($\epsilon_r = 2.65$, $\tan\delta = 0.001$) dielectric boards. The repetition period of the metallic fishbone structure along the x direction is p_x. The metallic fishbone structure consists of 44 blades with the blade length spatially modulated by $h(z)$. The corresponding propagation constant of the mediated SSPP $k_{\mathrm{SPP}}(z)$ grows from the smallest value to the highest value first, and then drops back to the smallest value. This specific design is just for wave-vector matching at the air-dielectric and dielectric-air interfaces. It guarantees high conversion efficiency between the SSPP and the free-space wave. Thus, the transmittivity based on SSPP coupling can be greatly enhanced. In the y-z plane, the repetition period of the fishbone structure along the y direction is a. The thickness of this PCM is t. The photograph of the fabricated LTC PCM sample (size: 240×240 mm^2) is shown in Fig. 3(b). The fishbone structures are fabricated using a print circuit board (PCB) technique first. Then the final PCM sample is achieved by assembling the fishbone structure array and the metallic plate array in orthogonal directions.

To analyze this LTC PCM, the copolarization transmission coefficients for x and y polarized waves' normal incidence are simulated. The simulated copolarization transmission coefficients for the x polarized wave's normal incidence when the consisted MPA is removed are also given in Figs. 3(c) and 3(d). Figure 3(c) gives the amplitudes of the copolarization transmission coefficients, and the phases are depicted in Fig. 3(d). It can be found that the amplitude of the copolarization transmission coefficient under the x polarized wave's normal incidence is approximately equal to 1 above the cut-off frequency of the planar waveguide $f_c = 5.7$ GHz. For the y polarized wave's normal incidence, the amplitudes of the copolarization transmission coefficients are nearly 1 below the asymptotic frequency of SSPP mediated on the highest metallic blade $f_{\mathrm{sspp}} = 13$ GHz. While the MPA is removed, the x polarized incidence wave will be highly transmitted in the whole frequency range. From the simulated copolarization transmission phases given in Fig. 3(d), we can find that the copolarization transmission phases φ_{yy} and φ_{xx} for the waves' normal incidence onto the designed PCM are all nonlinearly dispersive as a function of frequency, and the phase difference between the copolarization transmission phases under the y and x polarized wave incidence $\Delta\varphi = \varphi_{yy} - \varphi_{xx}$ is approximately equal to $\pi/2$ over a wide frequency range from 5 to 12.6 GHz. However, if the MPA in the designed PCM is removed, the copolarization transmission phase φ_{xx} will be linearly dispersive, thus the phase difference will be equal to $\pi/2$ only at a single frequency. According to the polarization conversion principle of the PCM given in section 2, we can conclude that high-efficiency LTC polarization conversion transmission will be achieved under u and v polarized waves' incidence in a wide frequency range from 7 to 12.6 GHz.

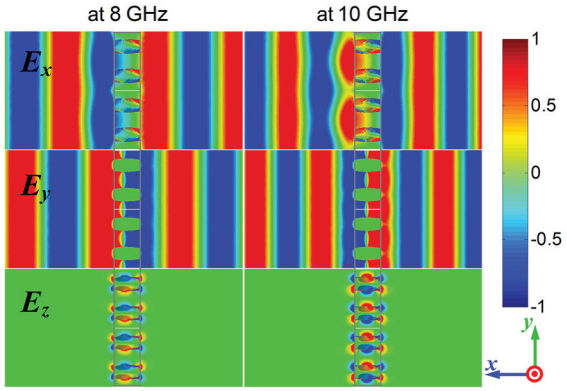

FIG. 4. Simulated electric field distributions in the *x*-*o*-*y* plane for the *u* polarized wave's normal incidence onto the LTC PCM from the +z direction at the frequencies $f = 8$ and 10 GHz.

To validate the polarization conversion transmissions of this LTC PCM, the LTC polarization conversion transmittivities (PCTs) under *u* and *v* polarized waves' normal incidence are calculated by full-wave numerical simulation as shown in Fig. 3(e). The measured LTC PCTs under the *u* polarized wave's normal incidence are given in Fig. 3(f). Obviously, the measured LTC PCTs are consistent with the simulated results in the whole frequency range. Both the simulated and measured results demonstrate that the LTC PCTs are greater than −0.5 dB over a wide frequency range from 7 to 12.6 GHz.

To visualize the coupled SSPP mode and waveguide mode in the LTC polarization conversion process, the electric field distributions under the *u* polarized wave's normal incidence are simulated at frequencies of 8 and 10 GHz. Figure 4 shows the distributions of the electric field *x*, *y*, and *z* components in the *x*-*o*-*y* plane for the *u* polarized wave's normal incidence. It is found that the waveguide mode with the larger wavelength is coupled in the PCM for the incidence electric field *x* component. And the incidence electric field *y* component is efficiently coupled into SSPP with a smaller wavelength on the fishbone structure, which can be further confirmed by the distribution of the electric field *z* component. The electric field *z* component is entirely confined near the fishbone structure in the PCM. By comparison, we can find that the phase differences between the phase accumulations for the incidence electric *y* and *x* components are all $\pi/2$ at the two frequencies.

IV. CIRCULAR-TO-CIRCULAR POLARIZATION CONVERSION METAMATERIAL

The perspective view of the designed CTC PCM is shown in Fig. 5(a). In the same way, the MPA placed along the *y* direction is employed as a planar waveguide array to couple and guide the waveguide mode (fast

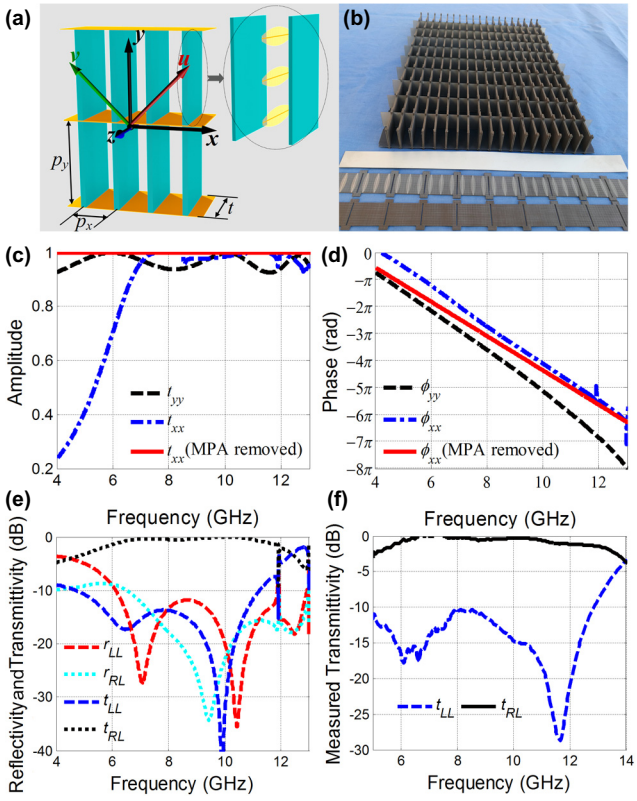

FIG. 5. (a),(b) Structural views of the CTC PCM: (a) perspective view of the designed CTC PCM ($t = 18$ mm, $p_y = 25.2$ mm, $p_x = 10$ mm, $a = 8.5$ mm, $d = 0.3$ mm, and $h = 0.762$ mm). (b) Photograph of the fabricated CTC PCM sample. (c),(d) Simulated copolarization transmission coefficients for the *y* and *x* polarized waves; normal incidence onto the designed CTC PCM together with the copolarization transmission coefficients for the *x* polarized wave's normal incidence onto the CTC PCM with the MPA being removed. (c) Amplitude of the simulated copolarization transmission coefficients. (d) Phase of the simulated copolarization transmission coefficients. (e) Simulated co- and cross-polarization reflectivities and transmittivities for the LCP wave's normal incidence onto the designed CTC PCM. (f) Measured co- and cross-polarization transmittivities for the LCP wave's normal incidence.

wave mode). The thickness of the metallic waveguide wall is *d*. The distance between the waveguide inner walls is p_y. The metallic fishbone structures placed in the *y*-*z* plane are employed as the SSPP-supporting structures, for which the repetition period in the *x* direction is p_x. The metallic fishbone (consisting of 60 metallic blades) structure is sandwiched between two 0.762-mm-thick dielectric substrates ($\epsilon_r = 6.15$, $\tan\delta = 0.0009$) with the repetition period *a* along the *y* direction. The thickness of this CTC PCM is *t*. The photograph of the fabricated CTC PCM sample (size: 240×240 mm^2) is shown in Fig. 5(b).

The copolarization transmission coefficients under the *y* and *x* polarized waves' normal incidence onto the designed

CTC PCM are simulated and the results are given in Fig. 5. The copolarization transmission coefficient for the x polarized wave's normal incidence onto the PCM with the MPA being removed is also depicted in Fig. 5 using the red solid line. Figure 5(c) gives the amplitudes of the simulated copolarization transmission coefficients. It can be seen that the incident y polarized wave can be highly transmitted below the cut-off frequency of the mediated SSPP on the longest metallic blade $f_{sspp} = 13$ GHz, and that the incident x polarized wave is highly transmitted above the cut-off frequency of the waveguide mode $f_c = 6$ GHz. The x polarized incidence wave is also highly transmitted in the whole frequency regime as the MPA in the PCM is removed. Figure 5(d) gives the phases of the simulated copolarization reflection coefficients. It is observed that the two copolarization transmission phases for the y and x polarized wave' normal incidence onto the CTC PCM (φ_{yy}, φ_{xx}) are all nonlinearly dispersive about the frequency, and the phase difference $\Delta\varphi = \varphi_{yy} - \varphi_{xx}$ is approximately equal to π over a wide frequency range from 4 to 11 GHz. According to the polarization conversion principle in Section 2, high-efficiency CTC polarization conversion can be achieved in a wide frequency range of 7.0–11 GHz. However, if the MPA in the designed PCM is removed, the copolarization transmission phase under the x polarized wave's normal incidence is linearly dispersive and the phase difference $\Delta\varphi = \varphi_{yy} - \varphi_{xx}$ is not a constant of π vs frequency. In this case, the CTC polarization conversion cannot be achieved in a wide frequency range.

To verify the high-efficiency CTC polarization conversion of the designed CTC PCM, the co- and cross-polarization reflectivities and transmittivities for the LCP wave's normal incidence are simulated and measured. Figure 5(e) gives the simulated co- and cross-polarization reflectivities and transmittivities for the LCP wave's normal incidence, and Fig. 5(f) shows the measured co- and cross-polarization transmittivities under the LCP wave's normal incidence. We find that the measured results agree well with the simulated results. Both the simulated and measured results indicate that the cross-polarization transmittivities are all greater than -0.5 dB under the LCP wave's normal incidence over a wide frequency range from 7 to 11 GHz. This is completely consistent with the previous theoretical analysis. The electric field distributions under the LCP wave's normal incidence at the frequencies $f = 8$ and 10 GHz are simulated as shown in Fig. 6. The distributions of the electric field x, y, and z components in the x-o-y plane are all depicted in Fig. 6. The simulated electric field distributions demonstrate that the waveguide mode with the larger wavelength is coupled in PCM for the x component of the incidence electric field. The electric field's y component distributions in the x-o-y plane indicate that the SSPP mode with the smaller wavelength is excited in PCM for the incidence electric field's y component. The coupled SSPP on the metallic fishbone

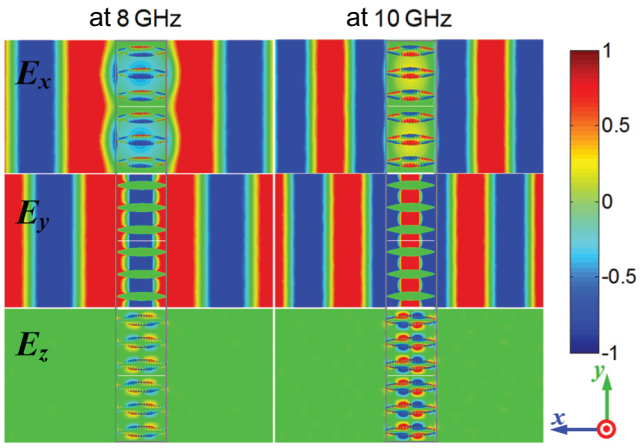

FIG. 6. Simulated electric field distributions in the x-o-y plane for the LCP wave's normal incidence onto the CTC PCM from the $+z$ direction at the frequencies $f = 8$ and 10 GHz.

structure is obviously visualized from the distribution of the electric field's z component. The phase differences between the phase accumulations of the SSPP mode and the waveguide mode observed from the electric field distributions are all approximately equal to π at the two frequencies.

V. CONCLUSION

In summary, high-efficiency polarization conversions for transmitted waves achieved by the synergy of fast wave and slow wave modes are proposed and demonstrated in this paper. The required phase differences between two orthogonal directions are realized via aligning the SSPP mode and waveguide mode in the two directions. Owing to the nonlinear dispersions of the SSPP mode and waveguide mode, the phase difference can be fixed at a certain value in a wider frequency regime by designing the dispersions of the SSPP mode and the waveguide mode. As a result, wideband polarization conversion may be achieved. To validate this method, two PCMs are designed, respectively, for LTC and CTC polarization conversions. The simulated and measured results indicate that the LTC PCTs are greater than -0.5 dB over a wide frequency range from 7.0 to 12.6 GHz, and the cross-polarization transmittivities under the CP wave's incidence are greater than -0.5 dB in a wide frequency range of 7.0–11.0 GHz.

ACKNOWLEDGEMENT

The authors are grateful for receiving support from the National Natural Science Foundation of China (NSFC) (Grants No. 61501503 and No. 61331005) and the Natural Science Foundation of Shaanxi Province under Grant No. 2017JM6005.

[1] Y. J. Chiang and T. J. Yen, A composite-metamaterial-based terahertz-wave polarization rotator with an ultrathin thickness, an excellent conversion ratio, and enhanced transmission, Appl. Phys. Lett. **102**, 011129 (2013).

[2] J. Hao, Y. Yuan, L. Ran, T. Jiang, J. A. Kong, C. T. Chan, and L. Zhou, Manipulating Electromagnetic Wave Polarizations by Anisotropic Metamaterials, Phys. Rev. Lett. **99**, 063908 (2007).

[3] J. B. Masson and G. Gallot, Terahertz achromatic quarter-wave plate, Opt. Lett. **31**, 265 (2006).

[4] N. Vieweg, M. K. Shakfa, and M. Koch, BL037: A nematic mixture with high terahertz birefringence, Opt. Commun. **284**, 1887 (2011).

[5] M. D. Feng, J. F. Wang, H. Ma, W. Mo, H. Ye, and S. B. Qu, Broadband polarization rotator based on multi-order plasmon resonances and high impedance surfaces, J. Appl. Phys. **114**, 074508 (2013).

[6] Y. F. Li, J. Q. Zhang, S. B. Qu, J. F. Wang, H. Y. Chen, Z. Xu, and A. X. Zhang,"Wideband selective polarization conversion mediated by three-dimensional metamaterials," J. Appl. Phys. **115**, 234506 (2014).

[7] X. Artiga, D. Bresciani, H. Legay, and M. J. Perruisseau-Carrier, Polarimetric control of reflective metasurfaces, IEEE Antennas Wireless Propagat. Lett. **11**, 1489 (2012).

[8] H. Chen, J. F. Wang, H. Ma, S. B. Qu, Z. Xu, A. Zhang, M. Yan, and Y. Li, Ultra-wideband polarization conversion metasurfaces based on multiple plasmon resonances, J. Appl. Phys. **115**, 154504 (2014).

[9] N. K. Grady, J. E. Heyes, D. R. Chowdhury, Y. Zeng, M. T. Reiten, A. K. Azad, A. J. Taylor, D. A. R. Dalvit, and H. T. Chen, Terahertz metamaterials for linear polarization conversion and anomalous refraction, Science **340**, 1304 (2013).

[10] Y. Zhao and A. Alù, Manipulating light polarization with ultrathin plasmonic metasurfaces, Phys. Rev. B **84**, 205428 (2011).

[11] H. L. Zhu, S. W. Cheung, K. L. Chung, and T. I. Yuk, Linear-to-circular polarization conversion using metasurface, Transactions on antennas and propagation **61**, 4615 (2013).

[12] S. Wu, Z. Zhang, Y. Zhang, K. Zhang, L. Zhou, X. Zhang, and Y. Zhu, Enhanced Rotation of the Polarization of a Light Beam Transmitted through a Silver Film with an Array of Perforated S-Shaped Holes, Phys. Rev. Lett. **110**, 207401 (2013).

[13] R. Z. Li, Z. Y. Guo, W. Wang, J. R. Zhang, A. J. Zhang, J. L. Liu, S. L. Qu, and J. Gao, high-efficiency cross polarization converters by plasmonic metasurface, Plasmonics **10**, 1167 (2015).

[14] H. Cheng, S. Chen, P. Yu, J. Li, L. Deng, and J. Tian, Mid-infrared tunable optical polarization converter composed of asymmetric graphene nanocrosses, Opt. Lett. **38**, 1567 (2013).

[15] J. Ding, B. Arigong, H. Ren, J. Shao, M. Zhou, and Y. K. Lin, Mid-infrared tunable dual-frequency polarization converters using graphene-based L-shaped nanoslot array, Plasmonics **10**, 351 (2015).

[16] H. F. Ma, W. X. Tang, Q. Cheng, and T. J. Cui, A single metamaterial plate as bandpass filter, transparent wall, and polarization converter controlled by polarizations, Appl. Phys. Lett. **105**, 081908 (2014).

[17] Q. Q. Zheng, Y. F. Li, J. Q. Zhang, H. Ma, J. F. Wang, Y. Q. Pang, Y. J. Han, S. Sui, Y. Shen, H. Y. Chen, and S. B. Qu, Wideband, wide-angle coding phase gradient metasurfaces based on Pancharatnam-Berry phase, Sci. Rep. **7**, 43543 (2017).

[18] S. C. Jiang, X. Xiong, Y. S. Hu, S. W. Jiang, Y. H. Hu, D. H. Xu, R. W. Peng, and M. Wang, High-efficiency generation of circularly polarized light via symmetry-induced anomalous reflection, Phys. Rev. B **91**, 125421 (2015).

[19] T. Cai, S. W. Tang, G. M. Wang, H. X. Xu, S. L. Sun, Q. He, and L. Zhou, High-performance bi-functional metasurfaces in transmission and reflection geometries, Adv. Optical Mater. **5**, 1600506 (2017).

[20] W. J. Sun, Q. He, J. M. Hao, and L. Zhou, A transparent metamaterial to manipulate electromagnetic wave polarizations, Opt. Lett. **36**, 927 (2011).

[21] W. J. Luo, S. L. Sun, H. X. Xu, Q. He, and L. Zhou, Transmissive Ultrathin Pancharatnam-Berry Metasurfaces with Nearly 100% Efficiency, Phys. Rev. Appl. **7**, 044033 (2017).

[22] C. Pfeiffer and A. Grbic, Metamaterial Huygens' Surfaces: Tailoring Wave Fronts with Reflectionless Sheets, Phys. Rev. Lett. **110**, 197401 (2013).

[23] C. Pfeiffer and A. Grbic, Millimeter-wave transmitarrays for wavefront and polarization control, IEEE Trans. Microwave Theory Tech. **61**, 4407 (2013).

[24] C. B. Liu, Y. Bai, Q. Zhao, Y. H. Yang, H. S. Chen, J. Zhou, and L. J. Qiao, Fully controllable pancharatnam-berry metasurface array with high conversion efficiency and broad bandwidth, Sci. Rep. **6**, 34819 (2016).

[25] J. B. Pendry, L. Martin-Moreno, and F. J. Garcia-Vidal, Mimicking surface plasmons with structured surfaces, Science **305**, 847 (2004).

[26] C. R. Williams, S. R. Andrews, S. A. Maier, A. I. Fernández-domínguez, L. Martín-moreno, and F. J. García-vidal, Highly confined guiding of terahertz surface plasmon polaritons on structured metal surfaces, Nat. Photonics **2**, 175 (2008).

[27] X. P. Shen and T. J. Cui, Planar plasmonic metamaterial on a thin film with nearly zero thickness, Appl. Phys. Lett. **102**, 211909 (2013).

[28] T. J. Cui and X. P. Shen, THz and microwave surface plasmon polaritons on ultrathin corrugated metallic strips, Terahertz Science and Technology **6**, 147 (2013).

[29] L. Chen, X. M. Ke, H. J. Guo, J. H. Li, X. Li, and L. Zhou, Broadband wave plates made by plasmonic metamaterials, Sci. Rep. **8**, 1051 (2018).

[30] Y. F. Li, J. Q. Zhang, S. B. Qu, H. Ma, J. F. Wang, J. Wang, and Z. Xu, High-efficiency polarization conversion based on spatial dispersion modulation of spoof surface plasmon polaritons, Opt. Express **24**, 24938 (2016).

[31] Y. F. Li, J. Q. Zhang, H. Ma, J. F. Wang, Y. Q. Pang, D. Y. Feng, Z. Xu, and S. B. Qu, Microwave birefringent metamaterials for polarization conversion based on spoof surface plasmon polariton modes, Sci. Rep. **6**, 34518 (2016).